Effect of thermal treatments on the catalytic behaviour in the CO preferential oxidation of a CuO–CeO2–ZrO2 catalyst with a flower-like morphology

Elisa Moretti (a), Loretta Storaro (a), Aldo Talon (a), Maurizio Lenarda (a), Piero Riello (b), Romana Frattini (b), María del Valle Martínez de Yuso (c), Antonio Jiménez-López (c), Enrique Rodríguez-Castellón (c), Fátima Ternero (d), Alfonso Caballero (d), Juan P. Holgado (d)

(a) INSTM – Dipartimento di Chimica, Università Ca' Foscari Venezia, Via Torino 155/B, 30172 Venezia, Italy

(b) Dipartimento di Chimica Fisica, Università Ca' Foscari Venezia, Via Torino 155/B, 30172 Venezia, Italy

(c) Departamento de Química Inorgánica, Cristalografía y Mineralogía (Unidad Asociada al ICP-CSIC), Facultad de Ciencias, Universidad de Málaga, Campus de Teatinos, E-29071 Málaga, Spain

(d) Instituto de Ciencia de Materiales de Sevilla (CSIC-University of Seville) and Departamento de Química Inorgánica, University of Seville, Avda. Américo Vespucio, 49, 41092 Sevilla, Spain

Abstract

A Ce–Zr–Cu oxide system with a flower-like morphology was prepared by a slow co-precipitation method in the absence of any structure directing agent. Four portions of the oxide were thermally treated at four different temperatures (350 °C, 450 °C, 550 °C, 650 °C). The resulting materials samples were characterized by quantitative XRD, adsorption–desorption of N2 at-196 °C, SEM and TEM microscopy, –H2-TPR, XPS and Operando-XANES. All samples were tested in the preferential CO oxidation (CO-PROX) in the 40–190 °C temperature range. Thermal treatments were found to induce slight structural changes without altering the starting morphology of the samples. The samples treated at higher temperature 550–650 °C showed a quite interesting CO-PROX activity and selectivity in a temperature range suitable for a practical use within the FEMFC technology.

Keywords

Hydrogen; CO-PROX; Copper; Ceria–zirconia; Flower-like morphology

1. Introduction

Hydrogen rich streams, in combination with fuel cells appear to be a viable energy alternative to fossil fuels both for mobile and stationary applications. In particular hydrogen fed proton-exchange membrane fuel cells (PEMFCs) can produce electrical

energy at low temperature (around 80 °C) with high efficiency, high power density and rapid start-up [1] and [2]. The reforming of alcohols and hydrocarbons is reasonably considered to be the most feasible method to produce large volumes of hydrogen-rich gas streams [3] and [4]. Nevertheless, PEMFC anode catalysts are highly sensitive to the presence of even traces of CO and therefore methodologies have to be developed for reducing CO contamination in the hydrogen feed. Currently, the simplest and most cost effective method to decrease the CO concentration down to ppm levels appears to be the preferential oxidation of carbon monoxide (CO-PROX) [5] and [6]. Catalysts based on the closely interacting CuO–CeO2 couple, are not only promising for their high activity and selectivity, but also very interesting from an economical point of view [7], [8], [9], [10], [11], [12], [13], [14], [15], [16], [17], [18], [19], [20], [21], [22] and [23]. The performances of CuO–CeO2 based catalysts in CO-PROX appear to be improved by the presence of highly dispersed copper species on the ceria surface that favour the formation of oxygen vacancies at the copper–ceria boundaries, thus increasing the Cu reducibility [7] and [17]. It is well known that addition of ZrO2 to ceria improves its redox properties, oxygen – storage capacity and thermal resistance [24]. Various studies have been carried out on the system CuO–CeO2–ZrO2 as CO oxidation catalysts both in the absence and in the presence of H2[19], [25], [26], [27], [28], [29], [30], [31] and [32]. The performance of these three-components catalysts was found strongly dependent from the three oxides molar ratio and from the used preparation methodology [19], [25], [26], [27], [28], [29], [30], [31] and [32]. The CeO2–ZrO2 oxide system is not only a well known automotive three way catalyst [33], a very interesting soot and alkanes combustion catalyst [34] and [35], but it is also a potential ionic conductor and a material with promising optical and magnetic properties. Because these properties are peculiar of CeO2–ZrO2 nanostructures, many different synthesis methods have been developed for their preparation, such as forced co-hydrolysis [36], co-precipitation [37], sol–gel [38], thermal decomposition [39]. Herein we describe the preparation, multi-techniques characterization and catalytic activity in the CO-PROX evaluation of series of samples of a nano-structured Ce/Zr/Cu based oxide system with a flower-like morphology, thermally pre-treated at various temperatures.

2. Experimental

2.1. Reagents

All the materials used are Aldrich products and no further purification was carried out.

2.2. Sample preparation

A 0.30 M aqueous solution of K2CO3 was slowly added (0.4 ml min−1) to an aqueous solution of CuCl2·2H2O (1.4 mmol), CeCl3·7H2O (8.1 mmol) and ZrOCl2·8H2O (0.9 mmol) under stirring, until a pH value of 8.2 was reached. The resulting suspension was left to settle overnight, then centrifuged and washed with deionized water till the complete disappearance of chlorides (AgNO3 test). The entire sample was dried overnight at 80 °C (FCZCuNC) and then split in four fractions that were calcined for 5

h (3 °C min−1), up to 350 °C (FCZCu350), 450 °C (FCZCu450), 550 °C (FCZCu550) and 650 °C (FCZCu650), respectively.

The samples were identified by acronyms FCZCuX, where: F = flower like C = cerium; Z = zirconium; X after the symbol of the element Cu indicates the thermal treatment used after synthesis (i.e., NC identifies the sample only dried at 80 °C without successive calcination; 350 identifies the sample calcined at 350 °C; etc.).

The metal contents were determined by ICP-OES elemental analysis. The CeO2 content was calculated as 86.0 wt.%, the ZrO2 as 7.0 wt.% and the CuO as 7.0 wt.%.

2.3. Catalytic activity measurements

Catalytic activity tests were carried out in a laboratory flow apparatus with a fixed bed reactor operating at atmospheric pressure. The catalyst, with a defined particle size (0.050–0.110 mm), was introduced in a tubular Pyrex glass reactor (5 mm i.d.), placed in an aluminium heating block.

Before the catalytic experiments, the sample was heated in situ at 400 °C under flowing air for 1 h. The gas hourly space velocity (GHSV) was 22,000 h−1. The feed consisted of 1.25% CO, 1.25% O2 and 50% H2 (% vol.) balanced with He (purchased from SIAD). The effect of CO2 and H2O was examined in separate runs after addition of 15 vol.% CO2 and 10 vol.% H2O in the feed gas. To evaluate the effect of water vapour on the reaction, a 10 vol.% H2O was pumped by a HPLC pump (supplied by Jasco) into the reaction stream.

Calibration of the GC was done with a gas mixture containing 1% CO, 1% CO2, 1% O2 in He. When the effect of CO2 was examined, the GC calibration was done with 15 vol.% CO2 in He. The gas lines were heated at 110 °C, to avoid water condensation before the reactor inlet. An ice-cooled water condenser was used to trap the excess of water downstream of the reactor. A HP6890 GC gas chromatograph equipped with a thermal conductivity detector was used to analyze the outlet composition. A CP Carboplot P7 column was used, with helium as carrier. The temperature was varied in the 40–190 °C range, and measurements were carried out till a steady state was achieved. Both methanation and reverse water–gas-shift reactions were found to be negligible in our experimental conditions. The carbon monoxide (the detection limit for CO was 10 ppm) and oxygen conversions were calculated based on the CO (Eq. (1)) and O2 (Eq. (2)) consumption, respectively:

$$\text{CO conversion} \quad (\%) = \frac{n_{CO}^{in} - n_{CO}^{out}}{n_{CO}^{in}} \times 100$$

$$\text{O}_2 \text{ conversion} \quad (\%) = \frac{n_{O_2}^{in} - n_{O_2}^{out}}{n_{O_2}^{in}} \times 100$$

To compare the activity of the catalysts as function of the temperature, Tconv50% was estimated as the temperature at which the catalyst converted half of the fed CO.

The selectivity towards CO2 was estimated from the oxygen mass balance as follows (Eq. (3)):

$$\text{Selectivity} \quad (\%) = \frac{n_{CO}^{in} - n_{CO}^{out}}{2(n_{O_2}^{in} - n_{O_2}^{out})} \times 100$$

The excess oxygen factor (λ) is defined as (Eq. (4)):

$$\lambda = 2 \times \frac{n_{O_2}^{in}}{n_{CO}^{in}}$$

2.4. Characterization techniques

Inductively coupled plasma (ICP-OES) analyses were performed with a Perkin-Elmer Optima 3100 XL spectrometer.

Thermogravimetric analyses (TGA) were carried out with a Netzsch STA 409 instrument. The samples (0.010 g) were heated in an alumina crucible, at constant rate (10 °C min−1) in a stream of air (20 cm3 min−1) from 40 °C to 1000 °C.

X-ray powder diffraction patterns (XRPD) were obtained using a Philips X'Pert system with a Cu Kα radiation (λ = 1.54184 Å). The samples were disc shaped pressed powders and spectra were collected after calcination. The average dimension of the crystallites was determined by the Warren–Averbach's equation.

Nitrogen adsorption–desorption measurements were performed at liquid nitrogen temperature (−196 °C) with an ASAP 2010 apparatus of Micromeritics. The analysis procedure is fully automated and operates with the static volumetric technique. Before each measurement, the samples (0.1 g) were outgassed first at 130 °C for 12 h at 5 × 10−3 Torr and then at room temperature for 2 h at 0.75 × 10−6 Torr. The N2 isotherms were used to determine the specific surface areas through the BET equation (SABET), and the specific pore volume (Vs) calculated at p/p0 = 0.98.

Scanning electron microscopy (SEM) images were taken with a JEOL JSM-5600LV, operated at 20 kV and using secondary electrons to form the image. The sample was coated with a thin layer of gold.

Transmission electron microscopy (TEM) images were taken with a JEOL JEM-3010, operating at 300 kV, equipped with a GATAN (Warrendale, PA, USA) Multi-Scan CCD camera model 794 and an Oxford EDS microanalysis detector. A Gatan Model 613-DH specimen holder was used to cool the specimen down to liquid nitrogen temperature, in order to keep it stable under the electron beam.

Temperature-programmed reduction (H2-TPR) experiments were carried out using an AUTOCHEM 2910 instrument from Micromeritics. Approximately 0.1 g of freshly calcined catalyst was placed on top of wool glass in a quartz reactor. In order to remove contaminants, the powder was pre-treated in helium (20 cm3 min−1) to 350 °C for 1 h. After cooling to ambient temperature, TPR experiments were carried out in 10 vol.% H2/Ar (30 cm3 min−1) increasing the temperature from 40 °C to 800 °C (10 °C min−1), by a temperature programmable controller. A cryogenic trap consisting of a gel formed by adding liquid nitrogen to ethanol, in a Dewar flask, was used to prevent water from entering the detector.

X-ray photoelectron spectra (XPS) were collected using a Physical Electronics PHI 5700 spectrometer with non monochromatic Mg Kα radiation (300 W, 15 kV, 1253.6 eV) for the analysis of the core level signals of O 1s, Zr 3d, Ce 3d and Cu 2p and with a multi-channel detector. Spectra of powdered samples were recorded with the constant pass energy values at 29.35 eV, using a 720 μm diameter analysis area. During data processing of the XPS spectra, binding energy values were referenced to the C 1s peak (284.8 eV) from the adventitious contamination layer. The PHI ACCESS ESCA-V6.0 F software package was used for acquisition and data analysis. A Shirley-type background was subtracted from the signals. Recorded spectra were always fitted using Gauss–Lorentz curves, in order to determine the binding energy of the different element core levels more accurately. The error in BE was estimated to be ca. 0.1 eV. Short acquisition time of 10 min was used to examine C 1s, Cu 2p and Cu LMM XPS regions in order to avoid, as much as possible, photoreduction of Cu2+ species. Nevertheless, a Cu2+ reduction in high vacuum during the analysis cannot be excluded [40].

X-ray absorption spectra (XAS) were recorded at the BM25 beam line (SpLine) of the ESRF synchrotron (Grenoble, France). The spectra were acquired in transmission mode using a Specac infrared-transmission cell equipped with Kapton windows that allow in situ treatment of the sample under controlled gas mixtures and temperatures up to 500 °C. The sample was placed in a stainless steel holder directly in contact with the gas mixture atmosphere and resistively heated. The samples were pressed as self-supported wafers in a standard 13-mm die, using the optimum weight to maximize the signal-to-noise ratio in the ionization chambers. For energy calibration, a standard Cu foil introduced after the sample was measured at the same time. Typical EXAFS spectra of Cu K edge were recorded from 8800 to 10,000 eV, with a variable step energy value, with a minimum 0.5-eV step across the XANES region (8970–9010 eV).

Data from this region were normalized and derived analytically using standard algorithms (software FEFFIT), and treated without further processing.

For the reaction treatments, CO, H2 and O2 were diluted in He (1000 ppm, 2500 ppm, and 3%, respectively). Mass flow controllers were used for dosing the gases to the cell, using a total flow of 100 cm3 min−1. The catalysts were placed in contact with the mixture at room temperature, then heated up to the desired temperature (range from 40 °C to 190 °C).

3. Results and discussion

3.1. Scanning electron microscopy

All the FCZCuX samples (non-calcined and calcined) present a flower-like morphology, made up of long (>10 μm) and thin (about 200 nm) petals with quite homogeneous size and shape (Fig. 1a–e). In Fig. 1 the SEM micrographs of the FCZCu samples, taken after thermal treatments in the 80–650 °C temperature range, are shown. The morphology of the as prepared material, that was non-calcined but only heated at 80 °C (sample FCZCuNC, Fig. 1a) composed by nano-sheets assembled in a flower-like architecture, appears to be maintained even after prolonged thermal treatment up to 650 °C (Fig. 1b–e).

3D nanostructures with a flower like morphology have been described in the last years for various oxides, often showing interesting potential technological properties. A flower-like shaped Ce1−xZrxO2solid solution [41] was electrochemically grown, well formed flower-like nano-architectures of Cu2O [42], ZnO [43], Fe2O3[44], Co3O4[45] and recently of CeO2[46] have been prepared by slow hydrothermal processes in the presence of glycols. All these materials have more or less well formed micro flowers-like morphologies constituted by petals shaped as nano-rods or nano-plates extending outward from the centre of the microstructure. It was suggested that the 3D architectures must be generated by some type of self-assembly occurring while the crystal growth is progressing. The exact mechanism for the formation of these flowers is still unclear, but it appears that the growth of the flower like morphology does not need the direction of a template and it is generally suggested that the hierarchical flowerlike 3D structures are formed by homocentric self-assembling from first formed 2D arrangements under control of various factors, such as electrostatic and dipolar fields, van der Waals forces, hydrophobic interactions and hydrogen bonds [42], [44] and [47]. It is therefore quite interesting that the Cu/Ce/Zr three components oxide system, described in this work, was prepared by a simple room temperature very slow addition of a K2CO3 solution to an aqueous solution of the precursors salts, followed by a long crystallization step a RT, in the absence of glycols or other organic additives, generally used to hydrothermally prepare materials with this kind of nano-architectures [42], [43], [44], [45] and [46].

It is also known that rare earths, among which Ce ions can crystallize from solutions containing carbonate ions, as orthorhombic or hexagonal phases of hydroxycarbonates, constituted by alternate stacks of cations and carbonate anions [48] that sometimes are organized with shuttle-like, butterfly like or flower-like homocentric morphologies [49], [50] and [51].

3.2. Thermogravimetric analysis

The TG/DTG profile of the non calcined sample LCZCuNC (not shown) exhibits a total mass loss of 27 wt.%, that can be divided in two regions: a first one, up to ca. 200 °C, attributed to the desorption of physisorbed water on the surface of the sample and a

second region, from 200 °C to 350 °C, where the TG curve shows the highest slope, corresponding to a consistent mass loss (23 wt.%) centred at about 290 °C.

We can reasonably suppose that the addition of K2CO3 to the salts solution will lead to the formation of a mixture of Ce(III), Cu(II) and Zr(IV) hydrated carbonates and hydroxy-carbonates. Cerium hydroxy-carbonate, that is the predominant component, generally undergoes a thermal decomposition in a single step, producing ceria following reaction (5):

(5)

$$2Ce(OH)CO_3(s) + \tfrac{1}{2}O_2(g) \rightarrow 2CeO_2(s) + 2CO_2(g) + H_2O(g)$$

Based on the stoichiometry of this oxidative process, the theoretic mass loss should be about 21%, very close to the obtained experimental value. Furthermore the Ce(OH)CO3 decomposition temperature reported in the literature is ca. 290 °C [49] that corresponds to the centre of the found experimental TG curve.

3.3. X-ray powder diffraction

All the diffraction patterns of the calcined samples (Fig. 2) show the characteristic reflections of CeO2, that match well with the peaks of the cubic phase of the fluorite crystal structure in JCPDS database (No. 43-1002).

Only the samples treated at higher temperatures (550 °C and 650 °C) show the presence of very small peaks at $2\theta = 35.5°$ and 38.5°, due to small clusters of copper oxide (CuO) and some shoulders near the main peaks of CeO2 that can be assigned to a solid solution of CeO2–ZrO2 very rich in ZrO2 (Fig. 3).

A careful Rietveld study of the diffraction patterns allow us to obtain quantitative information on the composition and on the distribution of the different oxides. The composition of the solid solutions $Zr_xCe_{(1-x)}O_2$ can be studied using the Vegard law that relates the volume of the unit cell Vc to the ZrO2 content x: $Vc = 158.84(\pm0.16) - 24.12(\pm0.26)x$. This equation has been obtained using the crystallographic data of the ICSD database (see Appendix A, for details). The random substitution of Ce4+ ions with Zr4+ in the fluorite cubic structure reduces the cell volume because of the smaller size of the Zr ions, but the study of this solution is a complicated matter because the cerium oxide can be itself a solid solution of Ce2O3–CeO2 and in this case the size of the Ce3+ ion is larger than that of Ce4+ and this can mask the reduction of the unit cell due to Zr4+ [Ce4+ (0.092 nm), Ce3+ (0.1034 nm) and Zr4+ (0.079 nm)].

As regards the samples treated at lower temperatures (FCZCu350 and FCZCu450), the XRD pattern can be described using a single phase cubic CeO2 (see Rietveld fits in Supporting material). The cell volume of these samples is 159.3 ± 0.1 Å3 and 158.9 ± 0.1 Å3, respectively, while the cell volume of the pure CeO2 is 158.4 ± 0.2 (this value

has been obtained as the average value of data reported in selected JCPDS files (see Appendix A for details).

Both these samples have the cells slightly larger than pure CeO2 and this could be due to the presence of a small fraction of Ce3+ ions in the fluorite structure. The reduction of the cell size with the increasing temperature supports this hypothesis.

No Zr containing phase was observed in these two samples: zirconium oxide could be amorphous or present as extremely dispersed nano-structured phase. In any case, we cannot exclude the formation of a ZrO2/CeO2 solid solution (expected cell volume is 156.5 Å3 corresponding to x = 0.1) hidden by the contemporary presence of Ce3+ ions.

The samples treated at the higher temperature (FCZCu550 and FCZCu650) have different XRD patterns: both show the presence of three phases: a cubic CeO2–ZrO2 with a low content of ZrO2, a ZrO2 rich tetragonal CeO2–ZrO2 solid solution and CuO.

As regards the CeO2 rich phase the cell volumes are respectively 158.5 ± 0.1 Å3 and 158.4 ± 0.1 Å3 that means a solid solution ZrxCe(1−x)O2 with a low content of ZrO2: x = 0.015 ± 0.005 for FCZCu550 and x = 0.02 ± 0.005 for FCZCu650.

The second phase of these samples is described as a solid solution very rich in ZrO2. The cell volumes of these phases are respectively 145.9 ± 0.8 Å3 and 142.8 ± 0.7 Å3. These volumes correspond to a tetragonal solid solution ZrxCe(1−x)O2 with x = 0.54 ± 0.05 for FCZCu550 and x = 0.66 ± 0.03 for FCZCu650. The quantitative Rietveld analysis for these two samples is reported in Table 1.

Unlike the samples thermally treated at lower temperature, in this case we can see that ZrO2 mainly forms a tetragonal solid solution with CeO2. The Ce/Zr ratios can be evaluated by quantitative analysis and are 92.7/7.3 for FCZCu550 and 90.7/9.3 for FCZCu650. These values are very close to the 9/1 ratio, obtained by ICP-OES, indicating that the solid solution is constituted essentially by ZrO2 and CeO2 and that copper oxide does not participate in a significant way. In any case, we cannot completely rule out that part of copper is in a solid solution with ZrO2 and CeO2, causing the decrease of the CeO2 cell parameter. As regards the two samples treated at 550 °C and 650 °C, only a small fraction of copper seems to be present as CuO nano-crystals, with sizes of 14 and 20 nm respectively. It follows that a large fraction of the copper oxide is present as extremely dispersed nanoparticles or, owing to the small size of the Cu2+ ion, as interstitial punctual defects in the ceria lattice. The samples heated at higher temperatures (550 °C and 650 °C) are characterized by narrower peaks, suggesting an increase of the particles diameter with the increasing heating temperature. In fact, the average size of ceria crystallites, evaluated by means of the Warren–Averbach line profile analysis, is about 3.9 nm for the sample calcined at 350 °C, 6.0 nm for the one calcined at 450 °C, 10.2 nm for the one treated at 550 °C and 13.8 nm for the one calcined at 650 °C. The estimated errors for crystallite sizes are about 10%.

3.4. Nitrogen adsorption/desorption

The porous nature of the prepared materials was evaluated by N2 physisorption at −196 °C. The isotherms of the FCZCuX series belong, in the IUPAC classification, to the Type II profile, with a small hysteresis loop suggesting that the very slow co-precipitation led to the formation of mesoporous solids, with the mesoporosity must probably originated by interparticles voids. The four layered calcined samples show different specific surface area values: the heat treatment in fact, causes a decrease of the BET surface area from 102 m2 g−1 to 28 m2 g−1. Consistently, also the total pore volume decreases from 0.074 cm3 g−1 to 0.022 cm3 g−1 (Table 2).

3.5. H2-temperature programmed reduction (H2-TPR)

The materials were characterized by H2-TPR to evaluate the reducibility of copper species. Measurements were carried out on the fresh calcined materials using 10 vol.% H2/Ar (30 cm3 min−1) from 40 °C to 800 °C. H2-TPR profiles of the samples are displayed in Fig. 4 and the corresponding amounts of H2 consumption are reported in Table 2.

Cu–Ce mixed oxides, with different copper loadings, were investigated by many authors [52] and [53]: it was observed that a strong interaction can easily occur at the interface between highly dispersed copper oxide and ceria, with a consequent lowering of the CuO reduction temperature and, concurrently, with a partial reduction of ceria at relatively low temperatures [54] and [8].

In all the samples, the presence of two partially overlapped reduction peaks was observed in the range 85–300 °C, indicating at least two type of copper species, while CeO2 gave a very broad peak starting at 650 °C, and centred at about 750 °C, that accounts for a limited surface shell reduction of cerium atoms from +4 to +3 oxidation state: this can be related to a surface reaction probably forming oxygen vacancies [52] and [55]. The complete reduction of CeO2 to Ce2O3 cannot occur under the present conditions because higher temperatures are needed [56].

The molar ratio H2/Cu (Table 2) underlines that the H2 consumption is much higher than what is necessary for the theoretical complete reduction of copper in the samples, under the hypothesis that Cu goes from the oxidation state +2 to 0. Nevertheless, H2 uptake due to the reduction of the oxygen ions of the ceria surface cannot be attributable to only this contribute: most probably, in a wide temperature range hydrogen spillover on the support occurs, as suggested by Gatica et al. [57] for Cu–Ce based materials. Hydrogen spillover is a phenomenon of dissociative adsorption of hydrogen on the catalytic sites, followed by hydrogen diffusion. Some hydrogen atoms remain attached to the metal, while others diffuse to the oxide support that has no activity for dissociative hydrogen adsorption but is characterized by surface oxygen ions capable to reduce.

For instance, the deconvolution of the H2-TPR curve of the sample FCZCu650 is presented in Fig. 5. The profile is a quite complex combination of several broad peaks together with a long tail, and its deconvolution evidenced that the curve, in the range 50–300 °C, is composed of four overlapping peaks, here denoted as α, β, γ and δ.

A qualitative attribution of the TPR peaks to different copper species over ceria supports has been proposed by many authors: Luo et al. [58] and Avgouropoulos and Ioannides [59] proposed that the lowest and highest temperature peaks were due to finely dispersed CuO in interaction with ceria and larger CuO particles, respectively. Zou et al. [60] suggested, for the more complex H2-TPR profiles, the contribution of both copper clusters and isolated Cu2+ ions.

Here, we propose that the first peak (α) can be attributed to the reduction of highly dispersed copper oxide species, strongly interacting with ceria [61]. The β peak can be assigned to small two- and three-dimensional clusters of copper oxide weakly associated with the ceria. The third peak γ quite intense, can be ascribed to the presence of CuO both in solid solution or as interstitial/substitutional defect in the ceria lattice, with consequent reduction according to the mechanism:

(6)

$$Ce^{4+}–O–Cu^{2+}–O–Ce^{4+} + 2H_2 \rightarrow Cu^0 + 2Ce^{3+} + 2H_2O$$

The peak named δ could be ascribed to the reduction of Cu2+ ions of the bulk-type CuO particles.

Comparing the profiles of the four samples in the region of copper species reduction (50–300 °C), a shift towards lower temperatures can be observed while increasing the calcination temperature. The α peak, not detectable for the FCZCu350 and FCZCu450 samples, became visible for the FCZCu550 and FCZCu650 samples (Fig. 4). The formation of Cu species, responsible for the α peak, could be ascribed to the known mobility at high temperatures of the copper ions, present as interstitial/substitutional defects in the ceria lattice, that probably can migrate outside the cerium oxide network, becoming highly dispersed Cu ions, easily reducible for the intimate contact with CeO2.

3.6. CO preferential oxidation (CO-PROX)

The catalytic activity of the samples was evaluated in the CO-PROX reaction and the results of the experiments carried out in the 40–190 °C temperature range, using a synthetic reformate gas (1.25% CO, 1.25% O2, 50.0% H2, He balance), are presented in Fig. 6a and b.

The CO conversion, for all the catalysts, increases with the temperature and is more than 95% above 140 °C (Fig. 6b). The selectivity to CO2 (Fig. 6b) is 100% at 120 °C, namely, considering the reaction stoichiometry, the oxygen excess factor used and the

CO conversion values, the O2 consumption is exclusively attributable to oxidation of CO to CO2.

The different thermal treatment appears to have a significant influence on the catalytic performance of the Ce–Zr–Cu oxide system and samples with identical chemical composition (with 7.0% CuO), exhibit a quite different catalytic behaviour. The sample FCZCu650, calcined at 650 °C, that represents the highest pre-treatment temperature, displays the highest activity over the entire investigated temperature range. For example, at 80 °C, that is the usual PEM Fuel Cells operating temperature, the activity of FCZCu650 is at least twice the activity of the other three samples (Fig. 6a). The T50 value (temperature at which 50% CO conversion is observed) moves from about 90 °C for FCZCu550 to 70 °C for FCZCu650, with a 100% CO2 selectivity. Even more interesting, in view of a practical use, is the finding that the FCZCu650 sample shows, in the 100–120 °C range, a CO conversion between 85% and 98% with a 100% selectivity to CO2. This can be ascribed to the presence in this sample of the highest amount of easily reducible copper oxide (as evidenced by H2-TPR data), that is known to be the catalytically active species in the CO-PROX reaction [11].

3.6.1. Effect of the addition of CO2 and H2O on the CO-PROX activity and selectivity

High activity and selectivity are decisive for a real CO-PROX application, but there are other important factors which have to be considered as well, e.g. the effects arising from a more realistic composition of the reaction gas mixture. Since a catalyst of selective oxidation of CO must be resistant to CO2 and H2O, the most representative sample, FCZCu650, was tested in an H2-rich feed, also in the presence of both 15 vol.% CO2 and 10 vol.% H2O.

When CO2 and H2O were added to the gas stream, the T50 value moves to about 120 °C with a selectivity to CO2 of 98% (Fig. 7).

The effect of time on stream was studied using the FCZCu650 sample (not shown). The reaction was monitored for 150 h, maintaining the temperature constant at 115 °C, using GHSV = 22,000 h−1; $\lambda = 2$; 1.25% CO, 1.25% O2, 50% H2, He balance (% vol.). The catalyst showed a diminution of CO conversion from 98% to 94% within the first 6 h, remaining stable for the further operation time.

3.7. X-ray photoelectron spectroscopy

Photoelectron spectroscopy was used to obtain further information about the valence/oxidation state of the elements and the surface composition of the Ce–Zr–Cu mixed oxides by inspecting the spectral line shape and the intensities of the Ce 3d and Cu 2p core-level electrons. The samples were analyzed before and after a CO-PROX catalytic test.

The XPS spectra of Ce 3d for sample FCZCu650 fresh and used are shown in Fig. 8. It is well known that the interpretation of the core level Ce 3d spectra is not straightforward due to the hybridization between the Ce 4f levels and the O 2p states [62], [63], [64], [65], [66], [67] and [68]. Larachi et al. reported a detailed description of the XPS core level spectra of Ce4+ and Ce3+ of CeO2 and Ce2O3, respectively [69]. A favourable method which considers the relative intensity of the u0 (v0) and u′ (v′) peaks to the intensity of Ce 3d region was applied to estimate the reduction degrees of ceria [63], [64], [65], [66], [67], [68], [69] and [70]:

$$\text{Ce(III)} \quad (\%) = \frac{100 \times [S(u_0) + S(u') + S(v_0) + S(v')}{\sum [S(u) + S(v)]}$$

The Cured/CuO and Ce3+/Ce4+ atomic ratios are included in Table 3 where Cured is the amount of copper reduced species and CuO the amount of Cu(II) species forming part of the copper oxide layer. For the sample FCZCu650, the Ce3+/Ce4+ ratio slightly increases as expected, following on the catalytic reaction, from 0.21 to 0.27, due to the presence of H2 (50 vol.% in the stream) that causes a partial reduction of Ce4+.

This is clearly observed in Fig. 8, where the contributions coming from Ce3+ produce a modification of the spectrum.

The same fact is observed in the case of the other studied samples (Table 3). As the calcination temperature increased, the Ce3+/Ce4+ atomic ratio does not experience appreciable changes, indicating that the thermal treatment does not affect the oxidation degree of Ce3+ at the surface.

The Cu 2p core level spectra for sample FCZCu650 fresh and used are shown, as an illustrative example, in Fig. 9. The Cu L3MM signal for the studied samples was not included due to its low intensity since the irradiation times was very short to get an acceptable signal/noise spectrum. Large irradiation times, necessary to obtain a clear signal, produce a clear photoreduction of Cu2+[71]. The core level spectrum Cu 2p of the fresh FCZCu650 shows a main Cu 2p3/2 peak that can be decomposed in two contributions at 932.6 eV and 934.8 eV. These two peaks, according with the literature [72] could be ascribed to the presence of CuO particles (contribution at 934.8 eV) and reduced copper species or small clusters of copper (contribution at 932.6 eV) formed by the strong interaction between copper and ceria. After reaction the relative intensity of the contribution due to CuO at 934.8 eV decreases (Fig. 9), and the Cured/CuO increases in comparison with the fresh sample. Moreover, the intensity ratio of the shake-up satellite and the intensity of the Cu 2p3/2 peak (ICusat/ICu2p) were found almost unchanged after the catalytic test. These facts are also observed for the other studied samples. Samples FCZCu350, FCZCu450 and FCZCu550 show a much lower copper reduction degree than sample FCZCu650, indicating that only the thermal treatment at high temperatures produces an enhanced reduction of surface copper, and this can explain the differences in the obtained H2-TPR curves, and in particular the high catalytic performance of catalyst FCZCu650 at lower temperature.

The surface atomic ratios Cu/Ce and Zr/Ce have been calculated from XPS spectra (see Table 4) and compared with the composition of the bulk determined by ICP-OES elemental analysis. The atomic ratios Cu/Ce and Zr/Ce, determined by ICP, are 0.18 and 0.11, respectively. The surface atomic ratio Cu/Ce in the case of samples FCZCu350 and FCZCu450 is close to that found in the bulk. However, samples FCZCu550 and FCZCu650 before catalysis present values far from 0.18. The surface atomic ratio Zr/Ce is always much lower than that of the bulk (0.11). Perhaps, copper ions are interacting on Zr(IV) and this fact produces a covering effect which gives rise to a lower surface concentration of Zr. The high concentration of carbon comes from the adventitious carbon plus surface carbonate as detected at 289.0 eV. The presence of surface carbonate is very common in presence of lanthanide ions. The surface composition after catalysis is more or less similar to that found for fresh catalysts, except in the case of sample FCZCu650 where a decrease of the copper content is observed.

3.8. Operando-XANES

Operando-XANES allows to study the oxidation states and the coordination of copper in the catalysts in real operating conditions. Recently, the behaviour of copper has been investigated by XANES in the CO-PROX reaction using nano-structured oxidized copper–cerium catalysts [73].

This work reports the presence of three different chemical species (Cu2+, Cu+ and Cu0) during the course of the runs. In Fig. 10a and b, the derivatives of the Cu K edge spectra for the catalyst FCZCu650 and FCZCu550, respectively, under CO-PROX reaction conditions (100 cm3 min−1, 50% H2, 1.2% CO, 1.2% O2, He balance) at different temperatures, are presented. In our case, at low reaction temperature, both the Cu2+ and Cu+ components predominate in the case of sample FCZCu650 (Fig. 10a). However, in the case of sample FCZCu550, the Cu2+ component, with a geometry similar to that of CuO, predominates (Fig. 10b). At higher reaction temperatures, the presence of Cu+ species slightly predominates with respect to Cu2+ species for sample FCZCu650, and metallic copper is detected at 190 °C. In the case of sample FCZCu550, the reduction of Cu2+ species to Cu+ with the increase of the reaction temperature is more moderate and the presence of Cu0 is hardly detected. The predominant presence of Cu+ in the reaction temperature range of catalytic interest (80–140 °C) in the case of sample FCZCu650 agrees with the XPS results where the maximum reduction of Cu2+ is observed (Table 3). These XANES results also support the hypothesis that the presence of Cu+ is a key factor to explain the observed improved catalytic activity of catalyst FCZCu650. XPS and XANES results explain the best catalytic performance of sample FCZCU650 but also the lower selectivity to CO2 at high reaction temperatures.

4. Conclusions

A Ce–Zr–Cu oxide catalyst with a flower-like morphology, was heat-treated at different temperatures (from 350 °C to 650 °C).

TEM micrographs show that the dimensions of the ceria/zirconia crystallites are less than 14 nm, indicating that the flower petals are polycrystalline structures. Powder XRD measurements show that in the thermally treated at high temperature samples, ZrO2 mainly forms a tetragonal solid solution with CeO2. The Ce/Zr ratio was evaluated by the quantitative analysis, and the values are very close to what obtained by ICP-OES. In the two higher temperature-treated samples (at 550 °C and 650 °C), only a small fraction of copper seems to be present as CuO nanocrystals, while a large fraction of the copper oxide is present as extremely dispersed nanoparticles or, owing to the small size of the Cu2+ ion, as interstitial punctual defects in the ceria lattice.

H2-TPR data point out that copper becomes progressively more easily reducible with the increasing temperature of the thermal treatment and this can be ascribed to the known mobility at high temperatures of the copper ions, present as interstitial/substitutional defects in the ceria lattice, that probably can migrate outside the cerium oxide network becoming highly dispersed Cu ions, that are easily reducible for the intimate contact with CeO2. The observed high value of the Cured/CuO ratio after the thermal treatment at 650 °C, pointed out by the XPS measurements, suggest the occurrence of surface segregation of reduced copper species in the samples treated at the highest temperature. Operando XANES showed the presence of all the three copper oxidation states, with a definite prevailing presence of the reduced species in the samples treated at the higher temperature. The very interesting CO-PROX activity and selectivity values, at relatively low temperatures, shown by the high temperature-treated samples, in particular by the FCZCu650 catalyst, can be attributed to the mobility at high temperatures of the small copper ions, that can migrate towards the surface becoming more easily reducible.

Appendix A. Vegard's law for the CeO2–ZrO2 solid solution

In order to characterize the solid solution of the two oxides and to obtain a calibration curve we have used the crystallographic data of the ICSD database. There are many files concerning this system that crystallizes both with cubic (fluorite type) and tetragonal structure depending on the ZrO2 content of the solid solution.

In order to have a single calibration line for cubic and tetragonal forms we have chosen to use the cell volume of the solid solution as composition dependent parameter. With this choice the volume of the conventional tetragonal cell has been doubled so both of the cells (cubic and tetragonal) contain the same number of metallic ions and fit together in a single line see Fig. 11.

In this analysis we have considered only the files collected at room temperature (see Table 6). Moreover we have not used the data obtained by multiphase samples (when specified in the comment line of the ICSD file).

The cell parameter of the cubic pure CeO2 ($a = 5.4107 \pm 0.0008$) has been obtained as the average value of the some recent ICSD files (see Table 6)

References

[1] A. Biyikoglu

Int. J. Hydrogen Energy, 30 (2005), p. 1181

[2] W. Schmittinger, A. Vahidi

J. Power Sources, 180 (2008), p. 1

[3] C. Song

Catal. Today, 77 (2002), p. 17

[4] J.R. Rostrup-Nielsen

Phys. Chem. Chem. Phys., 3 (2001), p. 283

[5] R.M. Navarro, M.A. Peña, J.L.G. Fierro

Chem. Rev., 107 (2007), p. 3952

[6] E.D. Park, D. Lee, H.C. Lee

Catal. Today, 139 (2009), p. 280

[7] D.H. Kim, J.E. Cha

Catal. Lett., 86 (2003), p. 107

[8] P.K. Cheekatamarla, W.S. Epling, A.M. Lane

J. Power Sources, 147 (2005), p. 178

[9] A. Martínez-Arias, A.B. Hungría, M. Fernández-García, J.C. Conesa, G. Munuera

J. Power Sources, 151 (2005), p. 32

[10] G. Avgouropoulos, T. Ioannides, H. Matralis

Appl. Catal. B, 56 (2005), p. 87

[11] G. Marbán, A.B. Fuertes

Appl. Catal. B, 57 (2005), p. 43

[12] A. Martínez-Arias, A.B. Hungría, G. Munuera, D. Gamarra

Appl. Catal. B, 65 (2006), p. 207

[13] T. Caputo, R. Pirone, G. Russo

Kinet. Catal., 47 (2006), p. 761

[14] E. Moretti, M. Lenarda, L. Storaro, A. Talon, R. Frattini, S. Polizzi, E. Rodríguez-Castellón, A. Jiménez-López

Appl. Catal. B, 72 (2007), p. 149 references therein

[15] Z. Liu, R. Zhou, X. Zheng

J. Mol. Catal. A, 267 (2007), p. 137

[16] M.J. Lippits, A.C. Gluhoi, B.E. Nieuwenhuiys

Topic Catal., 44 (2007), p. 159

[17] D. Gamarra, A. Hornés, Z. Koppány, Z. Schay, G. Munuera, J. Soria, A. Martínez-Arias

J. Power Sources, 169 (2007), p. 110

[18] E. Moretti, M. Lenarda, L. Storaro, A. Talon, T. Montanari, G. Busca, E. Rodríguez-Castellón, A. Jiménez-López, M. Turco, G. Bagnasco, R. Frattini

Appl. Catal. A, 335 (2008), p. 46

[19] E. Moretti, L. Storaro, A. Talon, R. Moreno-Tost, E. Rodríguez-Castellón, A. Jiménez-López, M. Lenarda

Catal. Lett., 129 (2009), p. 323

[20] E. Moretti, L. Storaro, A. Talon, M. Lenarda

Catal. Commun., 10 (2009), p. 522

[21] D. Gamarra, A. Martínez-Arias

J. Catal., 263 (2009), p. 189

[22] J.L. Ayastuy, A. Gurbani, M.P. González-Marcos, J.E. Herrero, J.M. Guil, M.A. Gutiérrez-Ortiz

Int. J. Hydrogen Energy, 34 (2009), p. 547

[23] (a) A. Gurbani, J.L. Ayastuy, M.P. González-Marcos, M.A. Gutiérrez-Ortiz

Int. J. Hydrogen Energy, 35 (2010), p. 1232

[23] (b) Int. J. Hydrogen Energy (2010), doi:10.1016/j.ijhydene.2010.04.045.

[24] P. Fornasiero, G. Balducci, R. Di Monte, J. Kašpar, V. Sergo, G. Gubitosa, A. Ferrero, M. Graziani

J. Catal., 164 (1996), p. 173

[25] P. Ratnasamy, D. Srinivas, C.V.V. Satyanarayana, P. Manikandan, R.S. Senthil Kumaran, M. Sachin, V.N. Shetti

J. Catal., 221 (2004), p. 455

[26] G.R. Kosmambetova, V.L. Gritsenko, P.E. Strizhak, A.M. Korduban

Theor. Exp. Chem., 42 (2006), p. 133

[27] M. Manzoli, R. Di Monte, F. Boccuzzi, S. Coluccia, J. Kašpar

Appl. Catal. B, 61 (2005), p. 192

[28] Y.-Z. Chen, B.-J. Liaw, H.-C. Chen

Int. J. Hydrogen Energy, 31 (2006), p. 427

[29] X.-F. Dong, H.-B. Zou, W.-M. Lin

Int. J. Hydrogen Energy, 31 (2006), p. 2337

[30] G. Aguila, F. Gracia, P. Araya

Appl. Catal. A, 343 (2008), p. 16

[31] V.P. Pakharukova, E.M. Moroz, V.V. Kriventsov, D.A. Zyuzin, G.R. Kosmambetova, P.E. Strizhak

Appl. Catal. A, 365 (2009), p. 159

[32] J. Zhu, L. Zhang, Y. Deng, B. Liu, L. Dong, F. Gao, K. Sun, L. Dong, Y. Chen

Appl. Catal. B, 96 (2010), p. 449

[33] J. Kašpar, P. Fornasiero, M. Graziani

Catal. Today, 50 (1999), p. 285

[34] E. Aneggi, C. de Leitenburg, G. Dolcetti, A. Trovarelli

Catal. Today, 114 (2006), p. 40

[35] S. Larrondo, M.A. Vidal, B. Irigoyen, A.F. Craievich, D.G. Lamas, I.O. Fábregas, G.E. Lascalea, N.E. Walsöe de Reca, N. Amadeo

Catal. Today, 107–108 (2005), p. 53

[36] M. Hirano, T. Miwa, M. Inagaki

J. Sol. State Chem., 158 (2001), p. 112

[37] A.S. Deshpande, N. Pinna, P. Beato, M. Antonietti, M. Niederberger

Chem. Mater., 16 (2004), p. 2599

[38] M. Alifanti, B. Baps, N. Blangenois, J. Naud, P. Grange, B. Delmon

Chem. Mater., 15 (2003), p. 395

[39] T. Masui, Y. Peng, K. Machida, G. Adachi

Chem. Mater., 10 (1998), p. 4005

[40] S. Poulston, P.M. Parlett, P. Stone, M. Bowker

Surf. Interface Anal., 24 (1996), p. 811

[41] G.-R. Li, D.-L. Qu, Y.-X. Tong

J. Phys. Chem. C, 113 (2009), p. 2704

[42] L.-L. Ma, J.-L. Li, H.-Z. Sun, M.-Q. Qiu, J.-B. Wang, J.-Y. Chen, Y. Yu

Mater. Res. Bull., 45 (2010), p. 961

[43] S. Ashoka, G. Nagaraju, C.N. Tharamani, G.T. Chandrappa

Mater. Lett., 63 (2009), p. 873

[44] L.-S. Zhong, J.-S. Hu, H.-P. Liang, A.-M. Cao, W.-G. Song, L.-J. Wan

Adv. Mater., 18 (2006), p. 2426

[45] L.-X. Yang, Y.-J. Zhu, L. Li, L. Zhang, H. Tong, W.-W. Wang, G.-F. Cheng, J.-F. Zhu

Eur. J. Inorg. Chem. (2006), p. 4787

[46] H. Li, G. Lu, Y. Wang, Y. Guo, Y. Guo

Catal. Commun., 11 (2010), p. 946

[47] J. Yang, C. Li, X. Zhang, Z. Quan, C. Zhang, H. Li, J. Lin

Chem. Eur. J., 14 (2008), p. 4336

[48] G. Adachi, N. Imanaka, Z.C. Kanng (Eds.), Binary Rare Earth Oxides, Springer (2004)

[49] M. Jobbàgy, C. Sorbello, E.E. Sileo

J. Phys. Chem. C, 113 (2009), p. 10853

[50] Z.H. Han, N. Guo, K.B. Tang, S.H. Yu, H.Q. Zhao, Y.T. Quian

J. Cryst. Growth, 219 (2000), p. 313

[51] F. Gu, Z. Wang, D. Han, G. Guo, H. Guo

Cryst. Growth. Des., 7 (2007), p. 1452

[52] A. Pintar, J. Batista, S. Hočevar

J. Colloid Interface Sci., 285 (2005), p. 218

[54] M.F. Kundakovic, Stephanopoulos

J. Catal., 179 (1998), p. 203

[55] Y. Liu, T. Hayakawa, K. Suzuki, S. Hamakawa, T. Tsunoda, T. Ishii, M. Kumagai

Appl. Catal. A, 223 (2002), p. 137

[56] S. Piras, A. Colussi, A. Trovarelli, V. Sergo, J. Llorca, R. Psaro, L. Sordelli

J. Phys. Chem. B, 109 (2005), p. 11110

[57] J.M. Gatica, R.T. Baker, P. Fornasiero, S. Bernal, G. Blanco, J. Kaspar

J. Phys. Chem. B, 104 (2000), p. 4667

[58] M.F. Luo, Y.J. Zhong, X.X. Yuan, X.M. Zheng

Appl. Catal. A, 232 (1997), p. 121

[59] G. Avgouropoulos, T. Ioannides

Appl. Catal. B, 67 (2006), p. 1

[60] H. Zou, X. Dong, W. Lin

Appl. Surf. Sci., 253 (2006), p. 2893

[61] E. Moretti, L. Storaro, A. Talon, P. Riello, R. Frattini, M. Lenarda

Micropor. Mesopor. Mater., 116 (2008), p. 575

[62] J.P. Holgado, G. Munuera, J.P. Espinós, A.R. González-Elipe

Appl. Surf. Sci., 158 (2000), p. 164

[63] R. Bechara, A. Aboukais, J.P. Bonnelle

J. Chem. Soc. Faraday Trans., 89 (1993), p. 1257

[64] J. Silvestre-Albero, F. Rodríguez-Reinoso, A. Sepúlveda-Escribano

J. Catal., 210 (2002), p. 127

[65] M.L. Trudeau, A. Tschöpe, J.Y. Ying

Surf. Interface Sci., 161 (2000), p. 301

[66] J.P. Holgado, R. Alvarez, G. Munuera

Appl. Surf. Sci., 161 (2000), p. 301

[67] A. Holmgren, F. Ararnoush, F. Fridell

Appl. Catal. B, 22 (1999), p. 49

[68] A. Kotani, T. Jo, J.C. Parlebas

Adv. Phys., 37 (1988), p. 37

[69] F. Larachi, J. Pierre, A. Adnot, A. Bernis

Appl. Surf. Sci., 195 (2002), p. 236

[70] X. Tang, B. Zhang, Y. Li, Y. Xu, Q. Xin, W. Shen

Appl. Catal. A, 288 (2005), p. 116

[71] E. Basaldella, E. Tara, G. Aguilar-Armenta, M.E. Patiño-Iglesias, E. Rodriguez-Castellón

J. Sol Gel Sci. Technol., 37 (2006), p. 141

[72] G. Avgouropoulos, T. Ioannides

Appl. Catal. A, 244 (2003), p. 155

[73] A. Martínez-Arias, D. Gamarra, M. Fernández-García, A. Hornés, P. Bera, Z.S. Koppány, Z. Schay

Catal. Today, 143 (2009), p. 211

Figure captions

Figure 1. SEM images of the samples FCZCuX treated at: (a) 80 °C; (b) 350 °C; (c) 450 °C; (d) 550 °C; and (e) 650 °C.

Figure 2. XRPD patterns of the sample FCZCuX, treated in air flow at 350 °C; 450 °C; 550 °C and 650 °C.

Figure 3. XRD pattern and Rietveld fit of FCZCu650. Inset: detail of the phases present in the sample.

Figure 4. H2-TPR profiles of the samples FCZCuX after thermal treatment at 4 different temperatures (from 350 to 650 °C).

Figure 5. Deconvolution of the H2-TPR profile for the sample FCZCu650.

Figure 6. Dependencies of: (a) CO conversion and (b) selectivity to CO2 as a function of temperature. Operating conditions: GHSV = 22,000 h−1; λ = 2; 1.25% CO, 1.25% O2, 50% H2, He balance (% vol.).

Figure 7. Variation of the (a) CO conversion and (b) selectivity towards CO2 as a function of temperature over the catalyst FCZCu650, in the absence and presence of 15 vol.% of CO2 and 10 vol.% H2O. Operating conditions: GHSV = 22,000 h−1; λ = 2; 1.25% CO, 1.25% O2, 50% H2, 0–15% CO2, 0–10% H2O, He balance (% vol.).

Figure 8. Ce 3d photoelectron profile of the sample FCZCu650: (a) fresh and (b) used.

Figure 9. Comparison between the Cu 2p photoelectron profiles for the samples LCZCu650: (a) fresh and (b) used.

Figure 10. Cu K edge Operando XANES spectra for the samples: (a) FCZCu650 and (b) FCZCu550, recorded during CO-PROX reaction, from 22 °C to 190 °C. Operating conditions: 1.25% CO, 1.25% O2, 50% H2, He balance (% vol.).

Figure 11. Variation of structure and cell volume of the solid solution CeO2–ZrO2 as function of ZrO2 content. The crystallographic data are obtained by ICSD files (see Table 5 and Table 6).

Table 1

Table 1. Quantitative Rietveld analysis of FCZCu550 and FCZCu650 samples.

Crystalline phase		**FCZCu550**		**FCZCu650**	
		x	**wt.%**	***x***	**wt.%**
Cubic	$Zr_xCe_{(1-x)}O_2$	0.015 ± 0.005	88.6 ± 0.7	0.02 ± 0.005	88.4 ± 0.5
Tetragonal	$Zr_xCe_{(1-x)}O_2$	0.54 ± 0.05	9.4 ± 1.0	0.66 ± 0.03	9.4 ± 1.0
Monoclinic	CuO	–	2.0 ± 0.3	–	2.2 ± 0.25

Table 2

Table 2. Nitrogen adsorption/desorption and H_2-TPR data of the prepared samples after different thermal treatments (BET specific surface area, pore volume, H_2 consumption, H_2/Cu molar ratio).

Sample	**Thermal treatment (°C)**	**SA_{BET} (m^2/g)[a]**	**V_p ($cm^3\ g^{-1}$)[b]**	**H_2 uptake (mol g^{-1} 10^{-3})**	**H_2/Cu (mol mol^{-1})**
FCZCu350	350	102 ± 1	0.074	1.42	1.61
FCZCu450	450	63 ± 1	0.062	1.26	1.44
FCZCu550	550	30 ± 1	0.046	1.13	1.28
FCZCu650	650	28 ± 1	0.022	1.08	1.21

a SA_{BET} = BET. Specific surface area.

b V_p = specific pore volume at p/p_0 = 0.98.

Table 3

Table 3. BE values (eV) and surface Cu_{red}/CuO and Ce^{3+}/Ce^{4+} atomic ratios before and after CO-PROX activity (GHSV = 22,000 h^{-1}; $\lambda = 2$; 1.25% CO, 1.25% O_2, 50% H_2, He balance).

Sample		**Cu 2*p*3/2**	***I*Cusat/*I*Cu 2*p*3/2**	**Cu_{red}/CuO**	**Ce^{3+}/Ce^{4+}**
FCZCu350	Before catalysis	932.2	0.53	0.41	0.25
		934.0			
	After catalysis	932.5	0.49	1.27	0.32
		934.1			
FCZCu450	Before catalysis	932.5	0.42	2.10	0.29
		934.7			
	After catalysis	932.2	0.49	2.60	0.32
		934.6			
FCZCu550	Before catalysis	932.6	0.53	1.05	0.22
		934.4			
	After catalysis	932.5	0.39	2.11	0.25
		934.6			
FCZCu650	Before catalysis	932.6	0.46	3.35	0.21
		934.8			
	After catalysis	932.4	0.48	4.00	0.27
		934.6			

Table 4

Table 4. Atomic concentrations (%) of the component elements of the FCZCu samples determined by XPS.

Sample		**C**	**O**	**Ce**	**Zi**	**Cu**	**Cu/Ce**	**Zr/Ce**
FCZCu350	Before catalysis	27.68	46.25	20.70	1.19	4.18	0.20	0.06
	After catalysis	22.31	51.94	21.03	1.12	3.58	0.17	0.05
PCZCu450	Before catalysis	26.63	46.57	21.46	1.44	3.91	0.18	0.07
	After catalysis	22.84	49.20	22.60	1.32	4.04	0.18	0.06
FCZCU550	Before catalysis	28.29	50.19	18.10	1.37	2.05	0.11	0.08
	After catalysis	30.70	47.91	17.80	1.36	2.24	0.13	0.08
FCZCu650	Before catalysis	26.39	45.58	20.03	1.34	6.65	0.33	0.07
	After catalysis	26.19	46.98	20.8	1.30	4.72	0.23	0.06

Table 5

Table 5. List of the selected ICSD files of the solid solution CeO_2–ZrO_2. *C*: cubic, *T*: tetragonal, *a* and *c*: cell parameters.

ICSD	***x* (ZrO_2 fraction)**	***a***	***c***	**Cryst. sys.**
–	0	5.41066	–	C
157415	0.38	5.311	–	C
164609	0.40	5.3049	–	C
161650	0.50	5.284	–	C
157416	0.31	5.3337	–	C
162790	0.10	5.386	–	C
152478	0.10	5.3846	–	C
157418	0.09	5.3857	–	C
157417	0.19	5.3619	–	C
152477	0.20	5.3669	–	C
162786	0.90	3.6239	5.2001	T
68590	0.82	3.64195	5.24403	T
164607	0.84	3.6377	5.2394	T
41579	0.88	3.6297	5.2217	T
89427	0.88	3.636	5.226	T
152471	0.85	3.6311	5.2166	T
75478	0.88	3.627	5.2336	T
162787	0.75	3.6679	5.2321	T
152472	0.60	3.7003	5.2634	T

Table 6

Table 6. List of the selected ICSD files of cubic CeO_2. *a*: edge of the cubic cell.

ICSD	***a***
61595	5.4109
621716	5.4037
621719	5.411
621707	5.411
72155	5.4124
88759	5.4112
156250	5.4116
157419	5.4113
246087	5.41

Figure 1

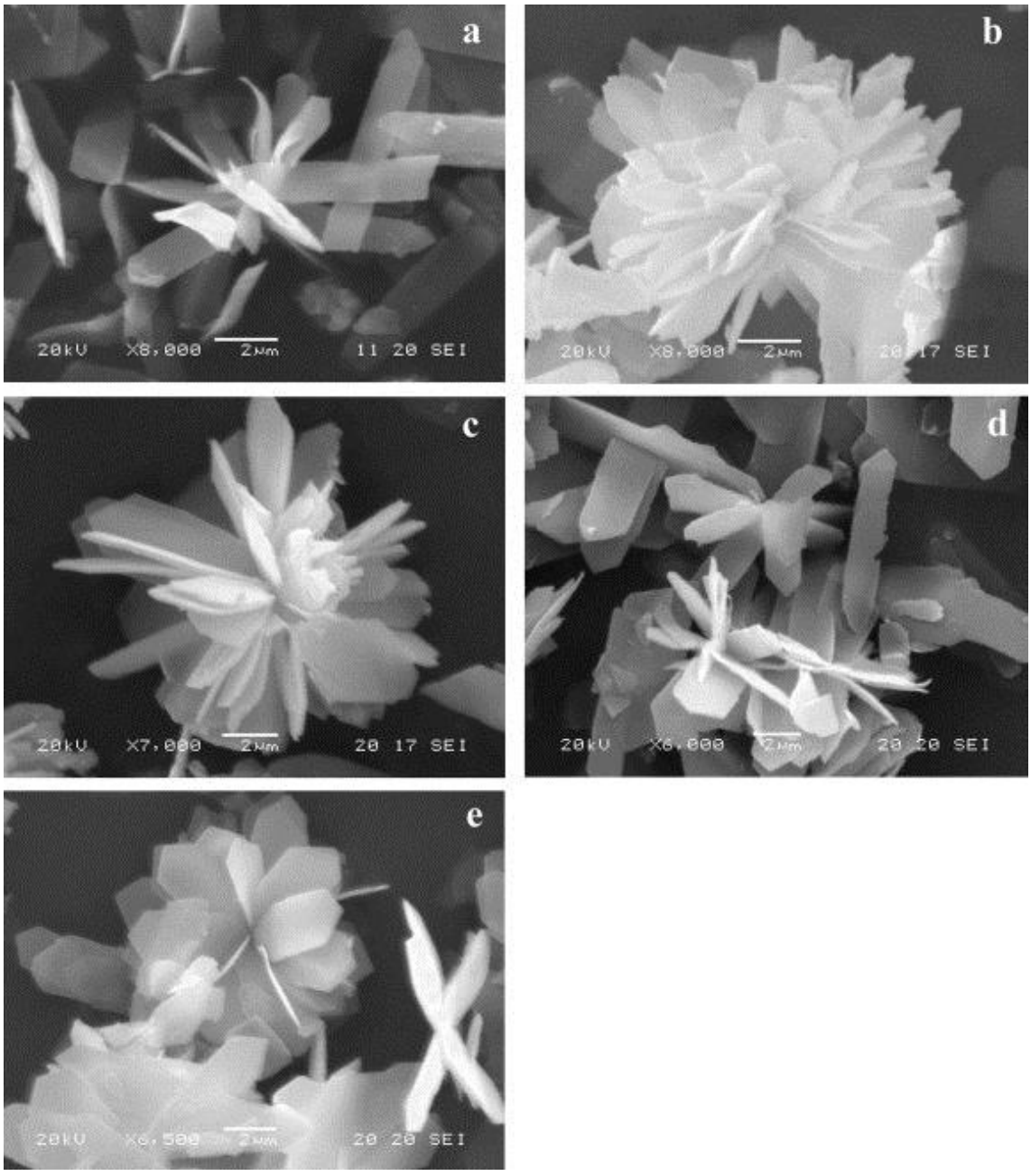
a
20kU X8,000 2μm 11 20 SEI
b
20kU X8,000 2μm 20 17 SEI
c
20kU X7,000 2μm 20 17 SEI
d
20kU X6,000 2μm 20 20 SEI
e
20kU X6,500 2μm 20 20 SEI

Figure 2

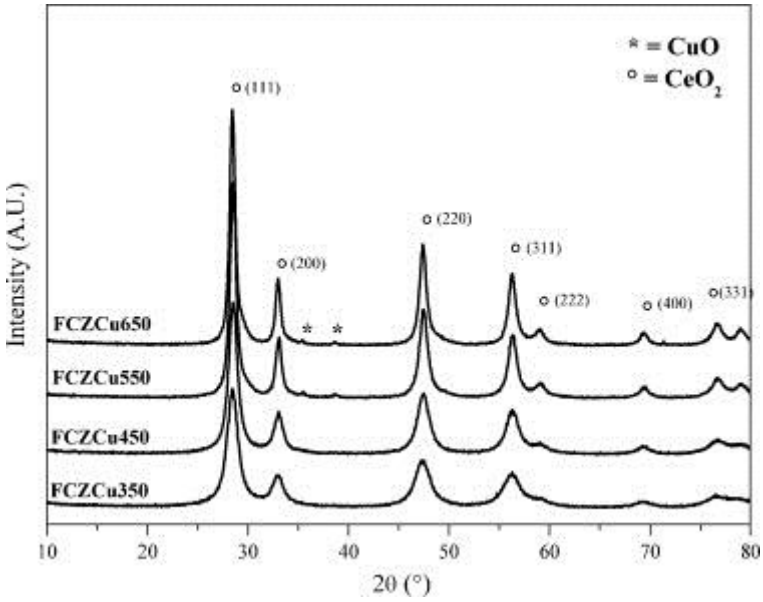
* = CuO
o = CeO2
o (111)
o (200)
o (220)
o (311)
o (222)
o (400)
o (331)
FCZCu650
FCZCu550
FCZCu450
FCZCu350
Intensity (A.U.)
10
20
30
40
50
60
70
80
2θ (°)

Figure 3

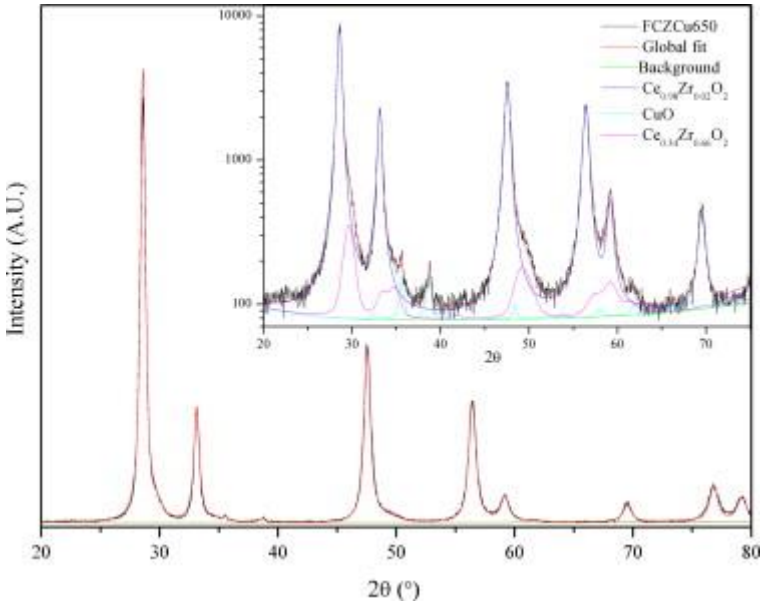

Figure 4

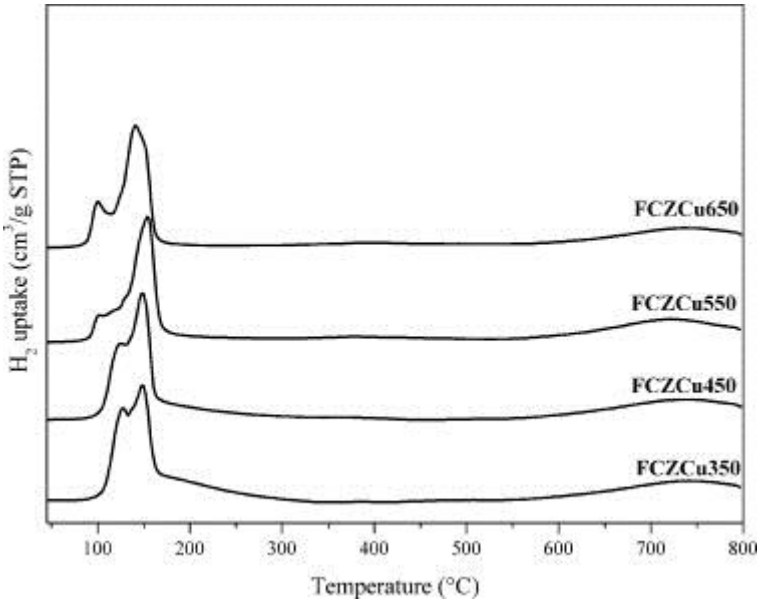
FCZCu650
FCZCu550
FCZCu450
FCZCu350
H2 uptake (cm3/g STP)
100
200
300
400
500
600
700
800
Temperature (°C)

Figure 5

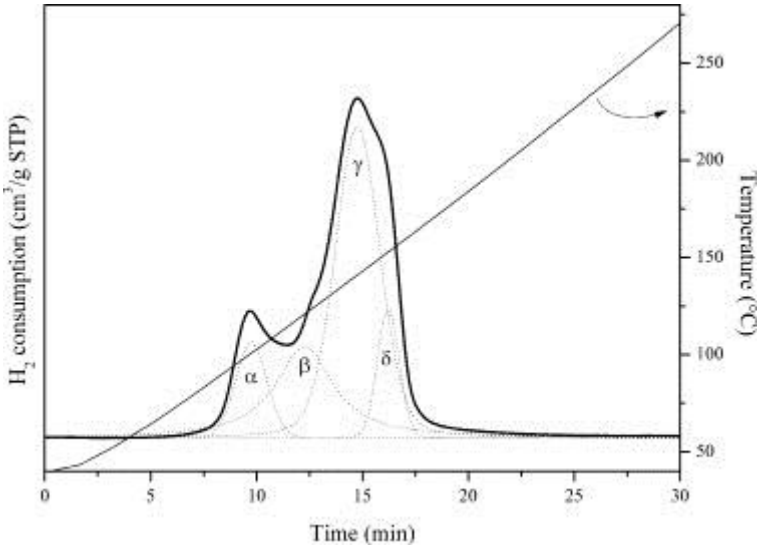
H2 consumption (cm3/g STP)
Temperature (°C)
Time (min)
α
β
γ
δ
0
5
10
15
20
25
30
50
100
150
200
250

Figure 6

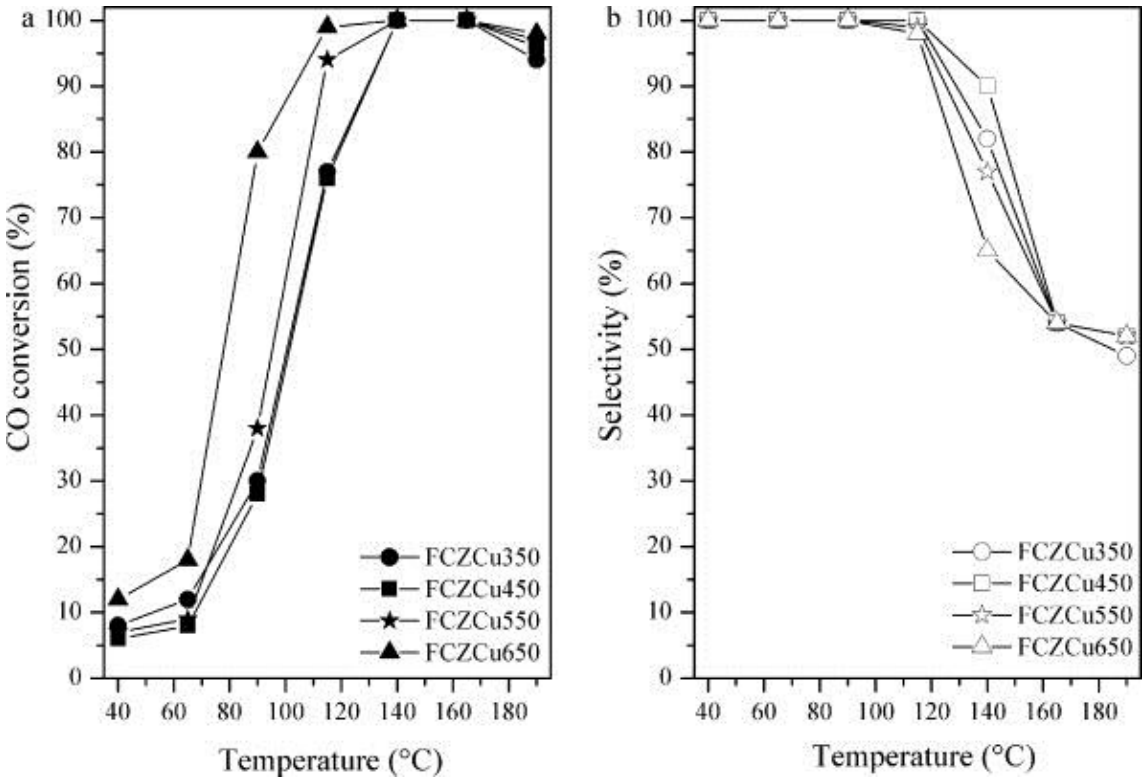
a
CO conversion (%)
Temperature (°C)
FCZCu350
FCZCu450
FCZCu550
FCZCu650
b
Selectivity (%)
Temperature (°C)
FCZCu350
FCZCu450
FCZCu550
FCZCu650

Figure 7

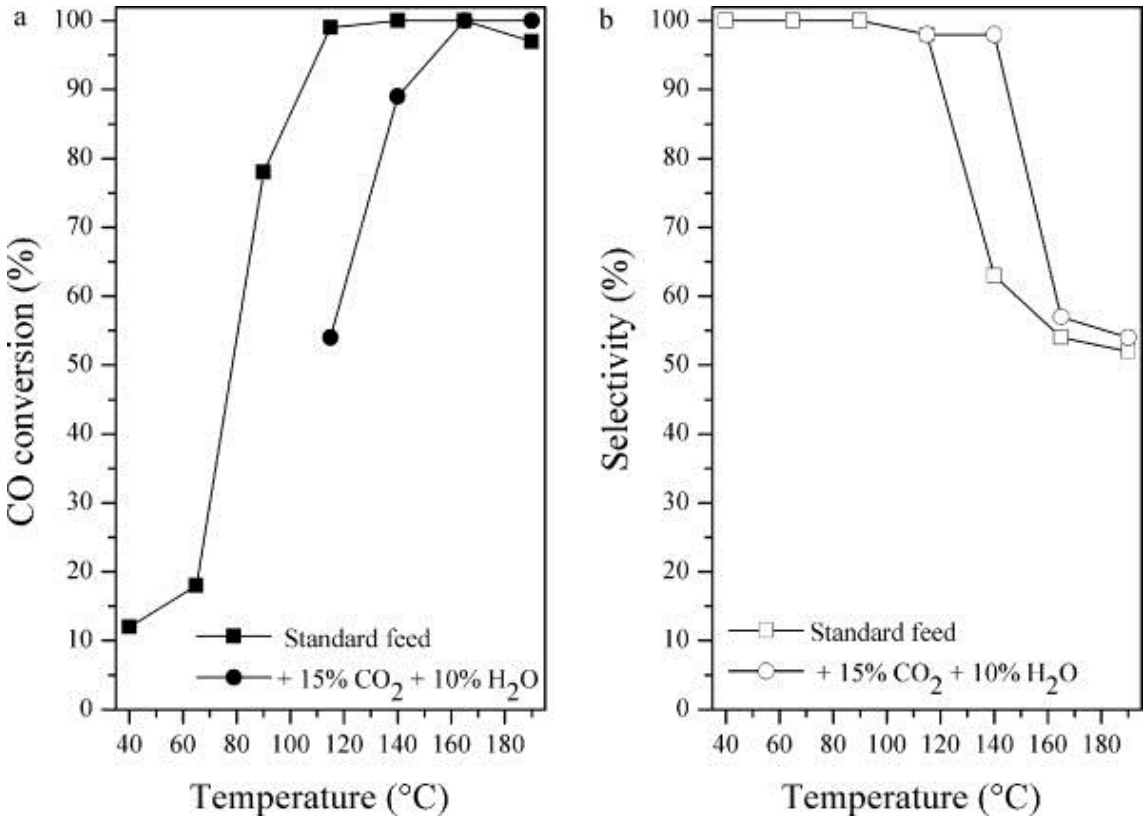
a
CO conversion (%)
Temperature (°C)
Standard feed
+ 15% CO2 + 10% H2O
b
Selectivity (%)
Temperature (°C)
Standard feed
+ 15% CO2 + 10% H2O

Figure 8

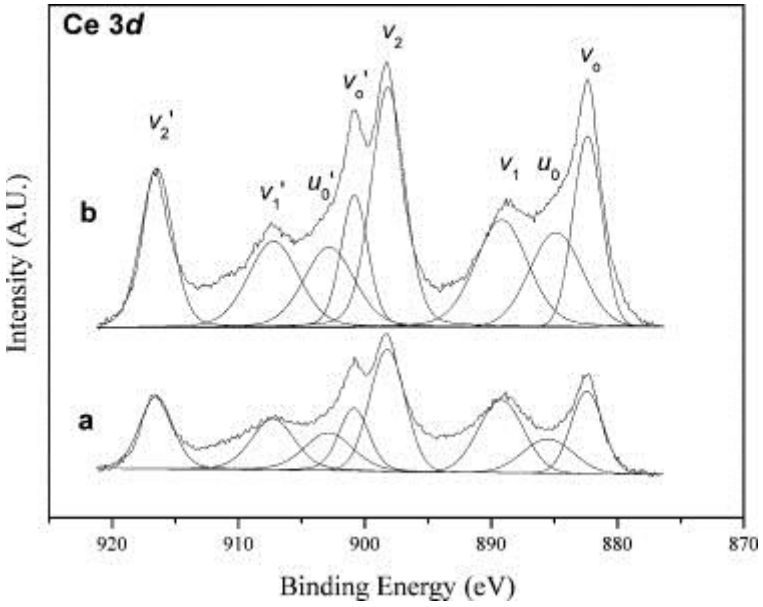
Ce 3d
v2'
v1'
u0'
v0'
v2
v0
v1
u0
b
a
Intensity (A.U.)
920
910
900
890
880
870
Binding Energy (eV)

Figure 9

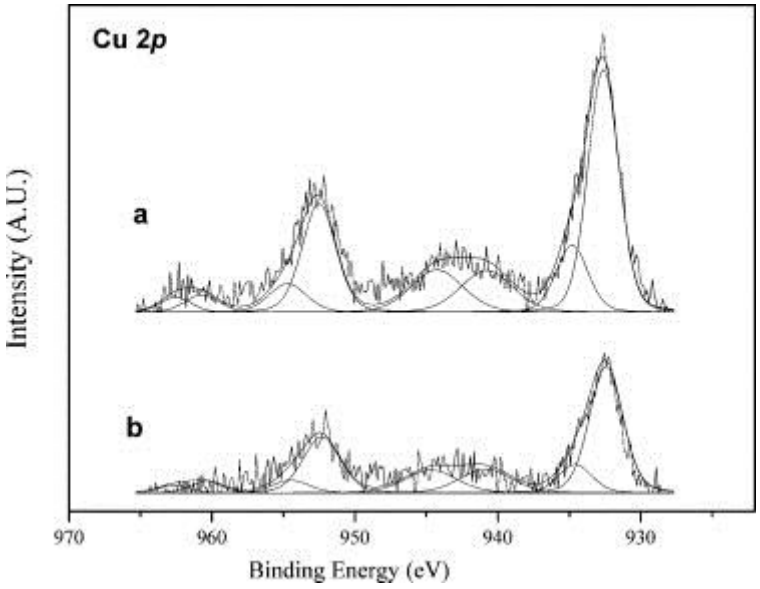

Figure 10

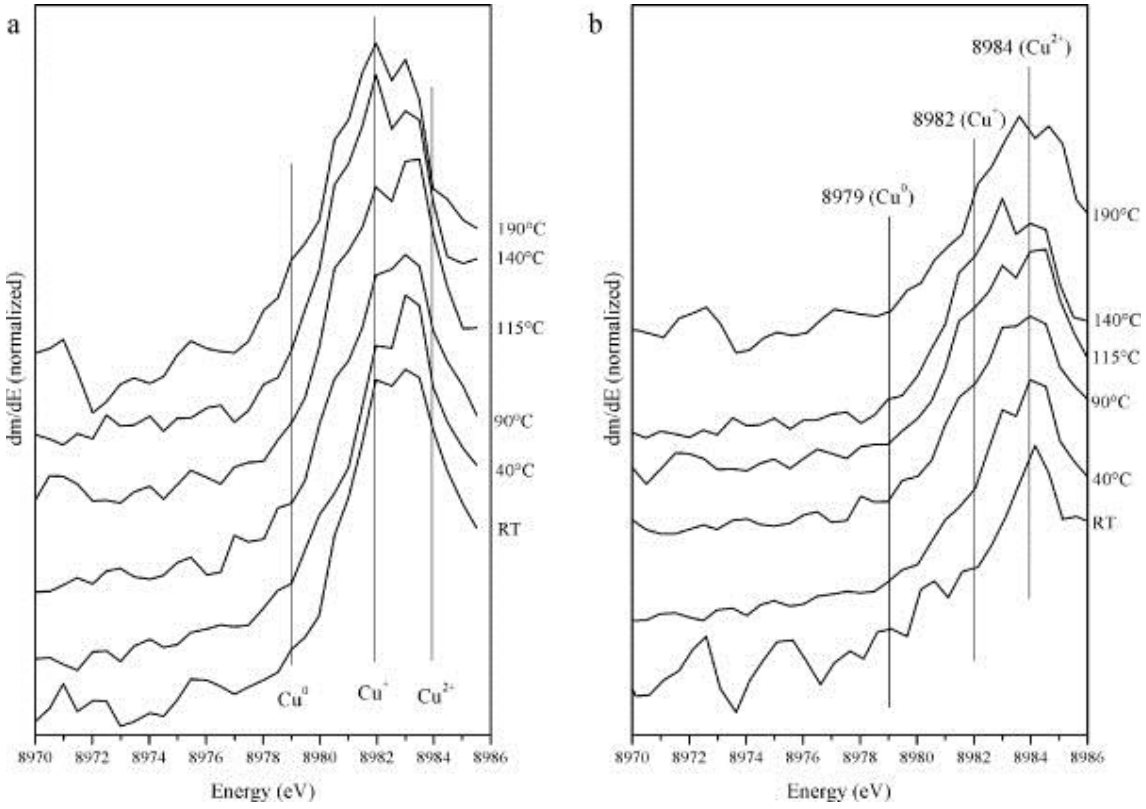
a
dm/dE (normalized)
190°C
140°C
115°C
90°C
40°C
RT
Cu0
Cu+
Cu2+
8970 8972 8974 8976 8978 8980 8982 8984 8986
Energy (eV)
b
8984 (Cu2+)
8982 (Cu+)
8979 (Cu0)
dm/dE (normalized)
190°C
140°C
115°C
90°C
40°C
RT
8970 8972 8974 8976 8978 8980 8982 8984 8986
Energy (eV)

Figure 11

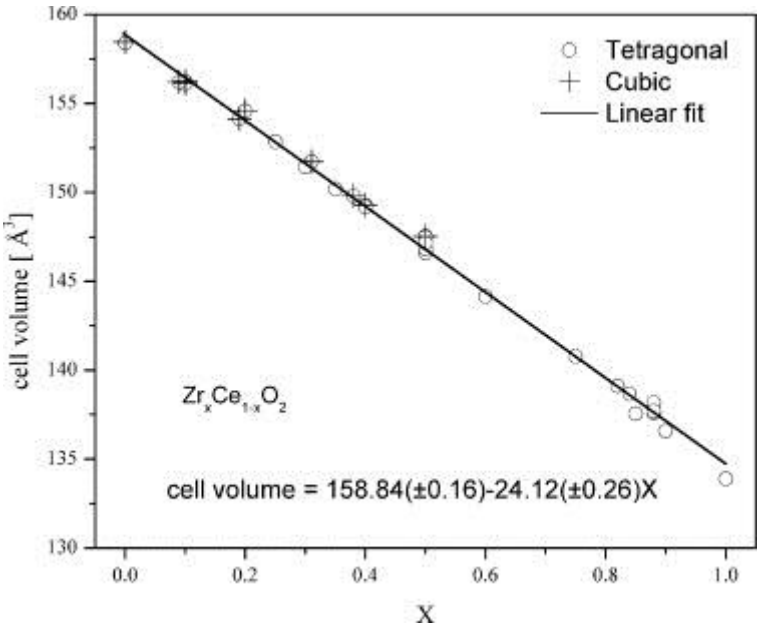
Tetragonal
Cubic
Linear fit
cell volume [Å^3]
$Zr_xCe_{1-x}O_2$
cell volume = 158.84(±0.16)-24.12(±0.26)X
X
160
155
150
145
140
135
130
0.0
0.2
0.4
0.6
0.8
1.0

Appendix B. Supplementary data